

WLM: Dynamics of an isolated Dwarf Irregular Galaxy Under Ram Pressure in the Local Group

Neel Kolhe¹, Francois Hammer¹, Yanbin Yang¹, Brenda Namumba², Laurent Chemin^{3,4}, Philippe Amram⁵, Roger Ianjamasimanana², and Claude Carignan^{6,7,8}

¹ LIRA, Observatoire de Paris, Université PSL, CNRS, Place Jules Janssen, 92195 Meudon, France
e-mail: neel.kolhe@obspm.fr

² Instituto de Astrofísica de Andalucía (CSIC), Glorieta de la Astronomía s/n, 18008 Granada, Spain

³ Université de Strasbourg, CNRS, Observatoire astronomique de Strasbourg, UMR 7550, 67000 Strasbourg, France

⁴ Instituto de Astrofísica, Departamento de Ciencias Físicas, Universidad Andrés Bello, Fernández Concha 700,

⁵ Aix Marseille Univ, CNRS, CNES, LAM, Marseille, France

⁶ Department of Astronomy, University of Cape Town, Private Bag X3, Rondebosch 7701, South Africa

⁷ Département de physique, Université de Montréal, Complexe des sciences MIL, 1375 Avenue Thérèse-Lavoie-Roux, Montréal, QC, Canada H2V 0B3

⁸ Observatoire d'Astrophysique de l'Université Ouaga I Pr Joseph Ki-Zerbo (ODAUO), BP 7021, Ouaga 03, Burkina Faso

February 10, 2026

ABSTRACT

WLM is an archetypal dwarf irregular galaxy that has not experienced interactions with major Local Group galaxies within the past 8 Gyr. It has recently been shown that WLM is losing its gas due to ram pressure forces exerted by the surrounding intergalactic medium (IGM). In this work, we explore how ram pressure may also affect the WLM gas kinematics, and we show that its dynamics is especially perturbed at its outskirts, explaining the asymmetric rotation between the approaching and receding sides. Moreover, we have been able to decompose WLM in two main components, a compact one with a solid-body rotation that resembles a bar-like structure, and a more extended one with a characteristic double-horn profile suggesting an edge-on disk. The former is relatively unaffected by ram pressure while the latter has its dynamics considerably affected by ram pressure. This study shows that mass estimates of a dwarf galaxy like WLM should account for a full modeling of its dynamical components, especially accounting for its asymmetric rotation curve.

Key words. Dwarf Irregular – Ram Pressure – Gaseous bar – Intergalactic medium

1. Introduction

The Wolf–Lundmark–Melotte (WLM) galaxy is an isolated gas rich dwarf irregular galaxy in the Local Group (LG) roughly 900 kpc away from the Milky Way and M31 (McConnachie, 2012). Within 1 Mpc, WLM is one of the dwarf galaxies that has not experienced interactions with the Milky Way or with M31 (Higgs et al. 2021). Owing to this spatial isolation throughout its evolutionary history, WLM has been a subject of extensive studies and has been characterized in the literature as a "prototypical irregular dwarf". In the hierarchical merger scenario of galaxy formation, dwarfs like WLM have merged to form larger galaxies like the Milky Way and M31. Hence studying an isolated dwarf like WLM gives us an insight into the properties of these progenitor dwarfs. Its high inclination has also made it a good candidate for dynamical studies (Hunter et al. 2012). However, the 70° inclination poses a challenge to determine features within the thick disk, which has also been described as an oblate spheroid.

WLM therefore has a rich history of being observed by flagship telescopes across frequencies. Recent JWST+HST studies have probed its star formation history (McQuinn et al. 2024; Albers et al. 2019), revealing steady star formation for the past 7 billion years, owing to its gas rich nature. Molecular clouds contributing to this star formation traced by CO cores have also been extensively studied by ALMA (Archer et al. 2022) and in

UV (Mondal et al. 2018). HI Radio observations have been performed with the VLA, GBT and the MeerKAT telescopes. They have provided us with an exquisite view into the neutral gas dynamics of WLM. For over a decade it has been noted in the literature, first by Kepley et al. (2007), that WLM shows a lopsided rotation curve on the approaching side of the galaxy. This triggered work to explain the asymmetry by considering a perturbed halo (Khademi et al. 2021), but this is not supported by the absence of past interactions for WLM.

Yang et al. (2022) found evidence of ram pressure stripping in the galaxy with the discovery of 4 trailing clouds detected by MeerKAT in the direction opposite of the galaxy's proper motion which was obtained from Gaia DR3 by Battaglia et al. (2022). They were also able to show that the clouds had no stars associated with them, confirming that the gas has been stripped through ram pressure. Yang et al. (2022) were able to replicate the orientation and mass of these stripped clouds using hydrodynamical simulations. They considered multiple models of WLM through various densities of the IGM and assuming varying WLM velocities with respect to the IGM, to constrain its density in the surroundings of the LG. McConnachie et al. (2007) have reported a similar occurrence of gas loss due to ram pressure induced by the IGM within the LG for the Pegasus dwarf galaxy (DDO 216), which is also an isolated body.

Table 1. Relevant Properties of WLM

Parameters	Symbol	Value	Units	Ref.
Optical Center	RA	00 ^h 01 ^m 58.2 ^s	-	1
-	DEC	-15° 27' 39'	-	1
Dynamical Center	RA	00 ^h 01 ^m 57.9 ^s	-	2
-	DEC	-15° 27' 12.26'	-	2
Systemic Velocity	V_{sys}	-126	km s^{-1}	2
Distance	d	0.934	Mpc	
Inclination	Inc	75.11	°	2
Position Angle	PA	175.5	°	2
Scale Height	H	0.4	kpc	3
Stellar Mass	M_{\star}	4.3×10^7	M_{\odot}	4
HI Mass (MK16)	M_{HI}	6.1×10^7	M_{\odot}	2
HI Mass (MK64)	M_{HI}	6.5×10^7	M_{\odot}	2
Comp 1 HI Mass	M_{HI}	3.4×10^7	M_{\odot}	2
Comp 2 HI Mass	M_{HI}	3.0×10^7	M_{\odot}	2

Notes. 1-Higgs et al. (2021). 2-This work. 3-Janamasimanana et al. (2020). 4-McConnachie (2012). Dynamical Center, Systemic Velocity, Inclination and Position Angle are derived from modelling presented in Section 4.

A large reservoir of baryonic matter in the universe is expected to be present in IGM filaments. Observational regimes ranging from Fast Radio Bursts to Lyman-alpha based methods have been used to put constraints on the cosmic IGM density (Connor et al. 2025; Jin et al. 2023). Intra-cluster medium of density 10^{-2} - 10^{-3} atoms/cm³ in large clusters has been studied and quantified using X-ray telescopes (Li et al. 2024). However, it is much sparser in less massive systems such as the LG, making it very hard to detect.

HI gas disks extend much farther beyond the stellar disks, especially for dwarf irregulars, and therefore, can be used to probe the total mass content of a galaxy to larger radii (Carignan & Freeman 1988; de Blok et al. 2008; Patra et al. 2016), under the assumption of dynamical equilibrium. In the case of WLM, an extreme dark matter (DM)-to-baryon ratio of 90:1 has been reported (Read et al. 2017). However, since the pioneering Gunn & Gott (1972) study, it is well established that the motion of galaxies through intragroup or intracluster medium perturbs their kinematics, particularly at the outer edges of their gaseous discs. Such interactions can drive the gas out of equilibrium, thereby biasing rotation curves and leading to systematic errors in the estimation of galactic masses. Therefore, having a thorough understanding of the DM halo extension and of the effect of the IGM on gas rich bodies is necessary to estimate the total mass content of dwarf irregulars.

There is growing evidence that ram pressure stripping due to the CGM of the Milky Way plays a major role in removing gas and transforming the dynamics of the Milky Way dwarfs (Hammer et al. 2024; Wang et al. 2024). Gas loss in WLM could also affect its dynamical evolution. The steady stripping of gas could also contribute to the two broad historical sub-classifications of isolated irregular dwarfs, those being gas rich and the other being mostly devoid of gas. Therefore, the goal of this paper is to use insights from state-of-art high velocity resolution 21cm radio observations of WLM from the MeerKAT telescope to study the kinematics for WLM and the effect of the IGM on gas dynamics.

In section 2 we revisit the Ianjammasimanana et al. (2020) MeerKAT 16 dish data to characterize the stripping gas more robustly and elaborate on the data reduction of the new MeerKAT 64 dish observations of WLM. In section 3, we look at the gas distribution in WLM and present a two-component Sersic fit. In section 4 we derive a rotation curve of WLM and discuss its dynamical properties. Section 5 elaborates on the kinematical decomposition in two components that we have performed on MeerKAT64 data, and in section 6 we discuss the consequences of our findings.

2. MeerKAT Observations

2.1. Revisiting the MeerKAT 16 dish Observations

Yang et al. (2022) used the observations from Ianjammasimanana et al. (2020), where they generated a mask by blanking pixels with values less than 3 times the RMS noise in the cube and used the MAFIA task in the MIRIAD software suite, leading them to detect the 4 stripped clouds. Motivated by trying to make a more robust detection of the stripped gas, we re-analysed the data cube with SoFiA-2 HI source finding tool. SoFiA-2 is optimised for HI surveys and can take into account noise variations and handles artifacts more reliably. We use the Smooth + Clip finder which iteratively smooths the cube with a defined set of spatial and spectral smoothing kernels, measuring the noise level at each smoothing scale and adding all pixels with an absolute flux density above a relative threshold (Serra et al. 2015; Westmeier et al. 2021). We set the source finding threshold to be 4 times RMS, and use spatial smoothing kernels of sizes 3, 6, 9, 12, 15, 18 pixels; as 3 pixels is just under the beam size and the smallest of the clouds detected by Yang et al. (2022) is roughly 18 pixels wide.

With the new SoFiA-2 mask applied to the data cube, we derive moment maps presented in Fig. 1. Instead of 4 isolated stripped clouds, we detect a continuous tail of stripped gas, akin to jellyfish galaxies (Roberts et al. 2021). For the main body of the galaxy, in the same region defined by Yang et al. (2022), we recover their total HI mass value of $6.1 \times 10^7 M_{\odot}$. However, Yang et al. (2022) have found a mass of $6.1 \times 10^6 M_{\odot}$ for the stripped gas, while we recover an improved $7.7 \times 10^6 M_{\odot}$.

Because we now see the tail of the stripped gas attached to the main body, we can also determine where the gas has been stripped from as we see a direct connection to the main body in the velocity field. The velocities distributions across the main body are clearly against the proper motion vector.

2.2. MeerKAT 64 Observation

Neutral hydrogen (HI) observations of the WLM galaxy were obtained with the MeerKAT radio telescope (Jonas 2018) as part of project SCI-20220822-BN-01, over two observing epochs on 2023 July 2–3 and July 3–4 (UTC). Observations were conducted in L-band 32k mode, which provides 32,768 frequency channels across an 856 MHz total bandwidth. For the purposes of HI spectral line imaging, a subset of 701 channels centered on the rest frequency of the HI line (1420.4058 MHz) was extracted, corresponding to a 2.289 MHz bandwidth. This yields a velocity coverage of $\sim 483 \text{ km s}^{-1}$ at a spectral resolution of 0.7 km s^{-1} per channel.

To map the HI distribution in and around WLM, we used an 11-pointing mosaic covering a rectangular area of $3^{\circ} \times 2.35^{\circ}$. The mosaic was arranged asymmetrically and extended toward the northwest, specifically designed to encompass several HI

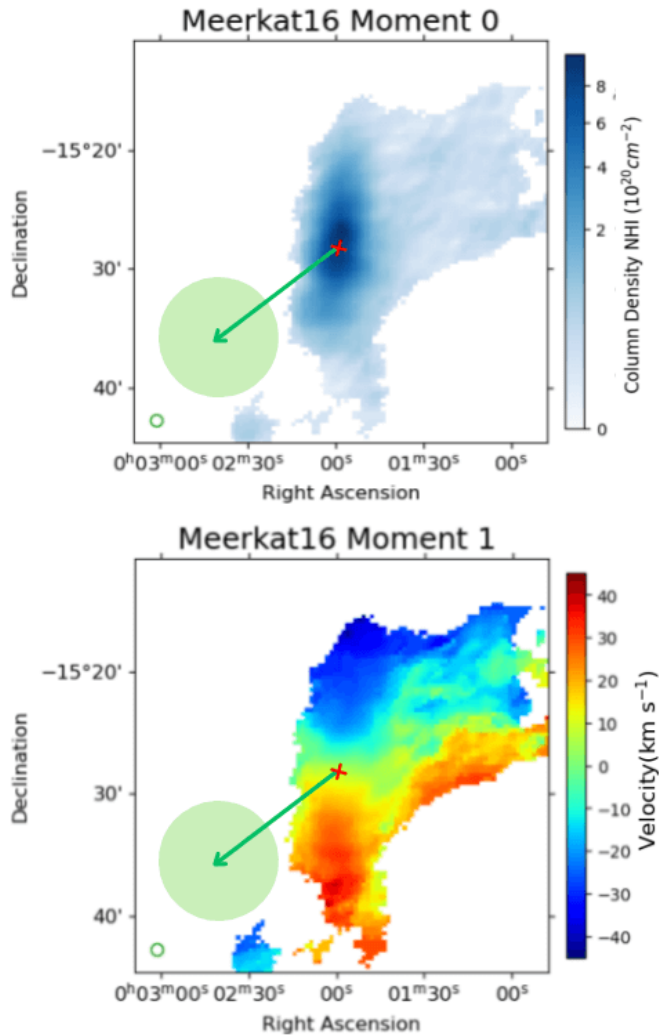


Fig. 1. Top and bottom panels show our new masked MeerKAT16 moment-0 and 1 maps of WLM. Both panels reveal the stripped H_I tail. The green arrow indicates proper motion and the transparent circle showing the 1σ uncertainty as presented in Battaglia et al. (2022) and Yang et al. (2022). The green circle at the bottom left marks the beam size.

clouds previously detected in lower-resolution MeerKAT-16 observations. This layout provided complete coverage of both the central disk and the surrounding low-column-density H_I environment. Each pointing was observed for a total integration time of approximately one hour. The primary flux and bandpass calibrator J1939–6342 was observed every 3 hours, while the complex gain (phase) calibrator J0025–2602 was observed approximately every 30 minutes.

The data was processed on a virtual machine of the Spanish Prototype of the Square Kilometre Array (SKA) Regional Center (espSRC, Garrido et al. 2021). Both observing epochs were calibrated using the Containerised Automated Radio Astronomy Calibration (CARACal) pipeline (Józsa et al. 2020). CARACal provides an environment to carry out standard calibration and reduction steps, including RFI flagging, cross-calibration, self-calibration, continuum subtraction, and imaging.

H_I spectral line imaging was performed individually for each pointing using WSClean (Offringa et al. 2014) as part of the CARACal pipeline. We followed a two-step iterative strategy to produce the final image cubes. In the first step, a low-

Table 2. H_I Observations and Imaging Parameters for the WLM Galaxy

Parameter	Value
Project code	SCI-20220822-BN-01
Observing dates	2023 Jul 2–4 (UTC)
Array configuration	MeerKAT (61 dishes)
Mosaic pointings	11
Band	L-band (856 MHz)
Spectral resolution	0.7 km s^{-1}
uv-taper (final cubes)	50''
Weighting	Robust 0.0
<i>Mosaic parameters</i>	
Synthesized beam	64'' \times 60''
RMS noise (single pointing)	0.0034 Jy beam $^{-1}$
RMS noise (mosaic)	0.0018 Jy beam $^{-1}$
Beam area scatter	3.78%
Flux density uncertainty	~7.6%
$3\sigma N_{\text{H}_1}$ sensitivity	$1.1 \times 10^{18} \text{ cm}^{-2}$

resolution cube was created using a Gaussian uv-taper of 90'' and brings Briggs robust weighting of 1.5, to enhance sensitivity to extended low-surface-brightness emission. These cubes were cleaned using WSClean’s automatic masking at a 5σ threshold, and the resulting masks were refined using SoFiA-2 (Westmeier et al. 2021) to isolate real emission structures. In the second step, the refined masks were applied to produce final cubes at higher resolution using a uv-taper of 50''. These final cubes were cleaned down to 0.5σ per channel, ensuring both completeness of faint emission and suppression of sidelobe artefacts.

The final data product is a linear mosaic composed of 11 pointings, each with a channel width of 0.7 km s^{-1} and a rms noise per channel of approximately 0.0034 Jy beam $^{-1}$, measured before primary beam correction. The mosaic was produced using CARACal, with primary beam correction applied during the mosaicing process. The resulting synthesised beam size is 64'' \times 60'', and the average rms noise in line-free regions of the central, primary-beam-corrected mosaic area is approximately 0.0018 Jy beam $^{-1}$ per 0.7 km s^{-1} channel. This imaging configuration was chosen to match the synthesised beam size of prior MeerKAT-16 observations, enabling direct comparison across datasets and resolutions.

To account for beam variations among individual pointings across the mosaic, we estimated a relative scatter in beam area of 3.78%, which leads to a maximum flux density uncertainty of approximately 7.6%. Considering this uncertainty and the achieved sensitivity, the mosaic provides a 3σ H_I column density sensitivity of approximately $1.1 \times 10^{18} \text{ cm}^{-2}$ over a 20 km s^{-1} linewidth in the central region. The observation setup and relevant parameters are summarized in Table 2.

The data was imaged with using natural weighting, several robust values, uv-tapers, and multi-scale deconvolution before settling on the above. The stripped gas detected in the earlier MEERKAT-16 observations was enabled by the compact 16-antenna configuration, which provided dense sampling at short baselines. In the 61-dish configuration used for our mosaic, the relative number of short spacings is significantly reduced, while the number of long baselines increases. This improves angular resolution but reduces sensitivity to large-scale, low-surface-brightness emission. We do not detect extended stripped faint structures with the 61 dish configuration, notably even features from the Magellanic Stream that appear clearly in single dish

GA3S observations (McClure-Griffiths et al. 2009) in the same velocity range of the mosaic field remain undetected, indicating that the limitation is intrinsic to the UV coverage rather than the imaging strategy. A full recovery of the diffuse tail would require combining our data with single-dish observations or acquiring targeted compact-configuration interferometric data. As this lies outside the scope of the present work, we plan to address the extended cloud in a dedicated follow-up study. While the reduced short-baseline sensitivity prevents recovery of these structures, including the diffuse tail, the 61-dish mosaic provides a high spectral resolution view of WLM's main body and the spatial resolution necessary for a detailed kinematic analysis. The final mosaic is once again processed with SoFiA-2 to generate a mask with the smooth+clip finder spatial kernels set to 0,3,6 and 0, 3, 7, 15 for the spectral axis with the cubelets feature turned on, which gives us individual data cubes for each continuous source. A threshold of $5 \times \text{RMS}$ was set for detection. The cubelet that detected the main body of the galaxy was chosen as the data source, which was used in the study. The generation of moment maps, column densities, flux and HI mass reported in Fig. 2 and elsewhere in this study follow the same procedure and formulae reported in Ianjamasimanana et al. (2020).

We recover a total flux density of 316 Jy km s^{-1} from our new observations, which corresponds to a total HI mass of $6.5 \times 10^7 M_\odot$ at a distance of 0.934 Mpc given in Higgs et al. (2021).

3. HI distribution in WLM

A visual inspection of our high resolution moment-0 map in Fig. 2 shows us that WLM has a dense central structure which tapers into the rest of the gaseous disk. This is also seen in the corresponding PV diagram in Fig. 3, where the dense gas core is seen along the steep velocity gradient at the center of the galaxy.

Higgs et al. (2021) found that the stellar radial profile of WLM in their g- and i-band survey is better fitted by 2 distinct morphological components instead of a single one, both components being described by a compact Sersic profile in the inner region and a shallower Sersic profile in the outer region. They tested whether a single component describes the profile better than two components by using the Akaike Information Criteria and the Bayesian Information Criteria. In their study for WLM a two-component model is almost 600 times more likely than the single component model, significantly favoring the two-component case. In the following, we repeat this test for the 1D gas profile of WLM.

Classical ellipse fitting to obtain a 1D HI flux profile may not work well for a galaxy at a very high inclination such as WLM. Therefore, we use two separate methods to extract the 1D profile; We perform the ELLPROF task in BBarolo (Teodoro & Fraternali 2015), which uses standard tilted-ring models, and we also implement the following simple procedure to get a profile to test for consistency.

The semi-major axis of the galaxy is determined by measuring the flux in the moment-0 map along a straight line along the PA reported in Table 1. The line is terminated when the flux reaches the $4 \times \text{RMS}$ noise in the moment map. The RMS noise in the map is determined by the noise in one channel multiplied by the square root of the number of contributing channels (Ianjamasimanana et al. 2018).

The semi-minor axis is calculated with the same procedure repeated along a line perpendicular to the PA along the center of the galaxy and thus an axis ratio is calculated. A central pixel is picked, corresponding to the chosen dynamical center, which is derived in Section 4.3, and ellipses are placed on the image,

their size starting with the axes lengths and then decreasing with a set value, while maintaining the axis ratio and PA of each. The image is broken into annular regions, with each ellipse being an annular boundary, mean flux is calculated for each region, so is the standard error on the mean value. Note that the ellipses are not being fit, they are determining spatial bin regions.

$$SE = \sigma / \sqrt{n} \quad (1)$$

In equation 1, SE , σ and n are the standard error, the standard deviation of the flux values and the number of pixels within each in the annulus, respectively.

Thus total uncertainty is calculated for each annulus with Eq. 2, with the RMS being calculated as described earlier in this section.

$$\text{uncertainty} = \sqrt{SE^2 + \frac{1}{n(\text{RMS}^2)}} \quad (2)$$

These values are then corrected for inclination presented in Table 1. Hence, we obtain the profile seen in Fig. 4, which is consistent with that obtained from the ELLPROF task in BBarolo. Thus, we can proceed to the Sersic modeling.

The Sersic profile is given by:

$$I(r) = I_e \exp\left(-b_n \left[\frac{r}{R_s}\right]^{1/n} - 1\right) \quad (3)$$

where $b_n = 1.9992n - 0.3271$ and I_e is the intensity at effective radius R_s and n is the Sersic index.

We fit a single-component Sersic model, and a two-component model to the derived profile and compare them with the Akaike information criterion (AIC) and Bayesian information criterion (BIC) as well (Burnham et al. 2010). Both methods provide us with a metric of comparison for fit models. However, BIC heavily penalizes large number of parameters, and hence can provide a counter against overfitting and is great to test out a two-component fit.

While comparing models, lower AIC and BIC values are preferred. AIC for the single component Sersic fit is 189.11 while for the two-component fit we have 57.42; AIC overwhelmingly supports the two-component fit. The BIC value for the single component fit is 28.65 and 22.49 for the two-component fit; in terms of probabilities given by:

$$P_i = \frac{e^{-\frac{1}{2}\Delta\text{BIC}_i}}{\sum_j e^{-\frac{1}{2}\Delta\text{BIC}_j}} \quad (4)$$

The two-component model is favored by a factor of 20 by BIC. Hence both criteria point to a two-component distribution of HI in WLM. Both in stars and gas, there are an inner compact component and an extended, more disk-like, outer component. The Sersic indices for the respective components are also in agreement as shown in the legend of Fig. 4 indicating that the two-components in both gas and stars are very similar.

In Section 4 we model the galaxy using the tilted ring method, however the model is applied separately for the approaching and receding sides owing to the galaxy's kinematic asymmetry.

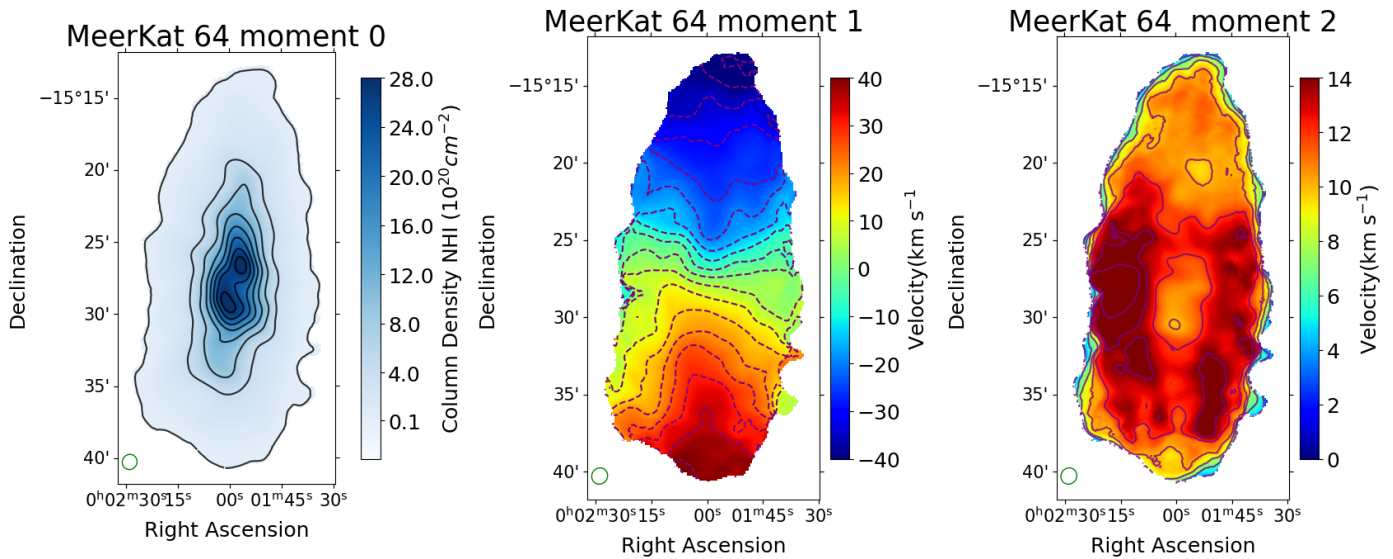


Fig. 2. HI high-resolution moment maps of MeerKAT 64 dish observation of WLM. All the figures are masked by our new MeerKAT64 moment-0 map (left panel). The contours of the moment-0 map correspond to the ticks of the colourbar. Central and right panels show respectively the rest frame moment-1 velocities and moment-2 dispersion map corrected from instrumental broadening. The contours of the moment-1 map correspond to a velocity range between -40 to 40 km s^{-1} with a spacing of 5 km s^{-1} and for the moment-2 map they correspond to $6,9$ and 12 km s^{-1} , respectively. The green circle shows the beamsize.

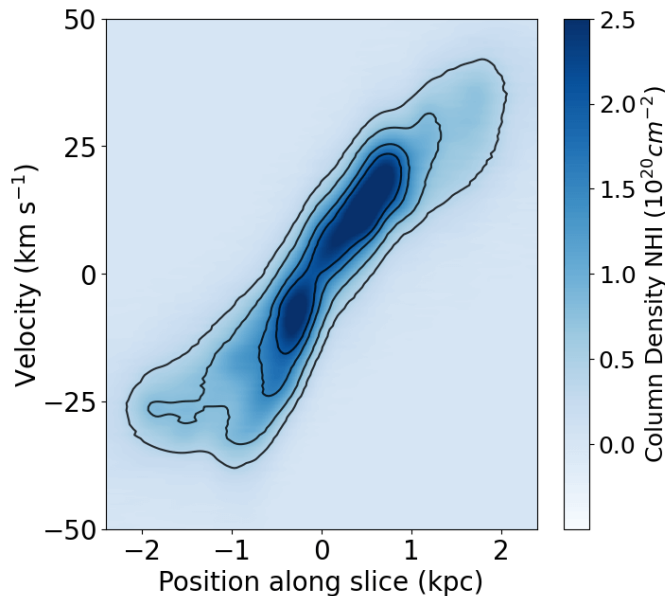


Fig. 3. Global PV diagram of WLM taken along the PA reported in Table 1. The contours correspond to the ticks on the colour bar.

4. Dynamics of WLM

4.1. The asymmetric Rotation Curve of WLM

Kepley et al. (2007) identified that WLM shows an asymmetric rotation curve on the approaching and receding sides. We can visually inspect the moment-1 map in Fig. 2 to see that the blue and the red side velocities show a symmetric rapid increase in the center, but the blue side ones taper down with sparsely packed contours while the red side keeps increasing rapidly.

The velocity contours in the moment-1 map significantly deviate from perpendicularity to the major axis, particularly in the central region. This, together with the fact that blue and red sides show different directions in the center could be a signature of a

dense bar-like structure at the center, and we discuss this later in Section 6.

The kinematic asymmetry is also apparent if we examine the PV diagram of WLM in Fig. 3, where the approaching side appears to flatten after 1 kpc while the receding side continues to rise.

Kepley et al. (2007) used a 2D tilted ring model to obtain the rotation curve on both sides of the galaxy separately. Within the first kiloparsec, the approaching side of the rotation curve rises above the receding side by 5 km s^{-1} , then the velocities cross over where the receding side rapidly rises like a solid body until the outskirts, while the approaching side shows a gentle rise. An asymmetric distribution of velocities is also apparent in the global velocity profile shown in Fig. 5, it points to a multi-component kinematic structure of the galaxy. This will be discussed in detail in section 5.

4.2. The expected impact of ram pressure to the asymmetric Rotation Curve

Yang et al. (2022) used the proper motion of WLM obtained by Battaglia et al. (2022) from Gaia DR3. The stripped gas is exactly in the opposite direction of the proper motion, which indicates that the ram pressure is applied in the same direction. As WLM moves through the IGM, its approaching side's motion, which contributes to the rotation curve, is aligned against the direction of ram pressure, while the receding side's motion is aligned along the direction of ram pressure. This scenario is depicted in Fig. 6.

4.3. The final Rotation Curve of WLM

To model the complex kinematics of WLM we adopt an iterative prescription based on the 3D tilted ring fitting tool TiRIFiC (Józsa et al. 2007). It allows for comprehensive disk modelling with a vast suite of available parameters to fit, with the possibility of granular control over the fitting procedure. We model the

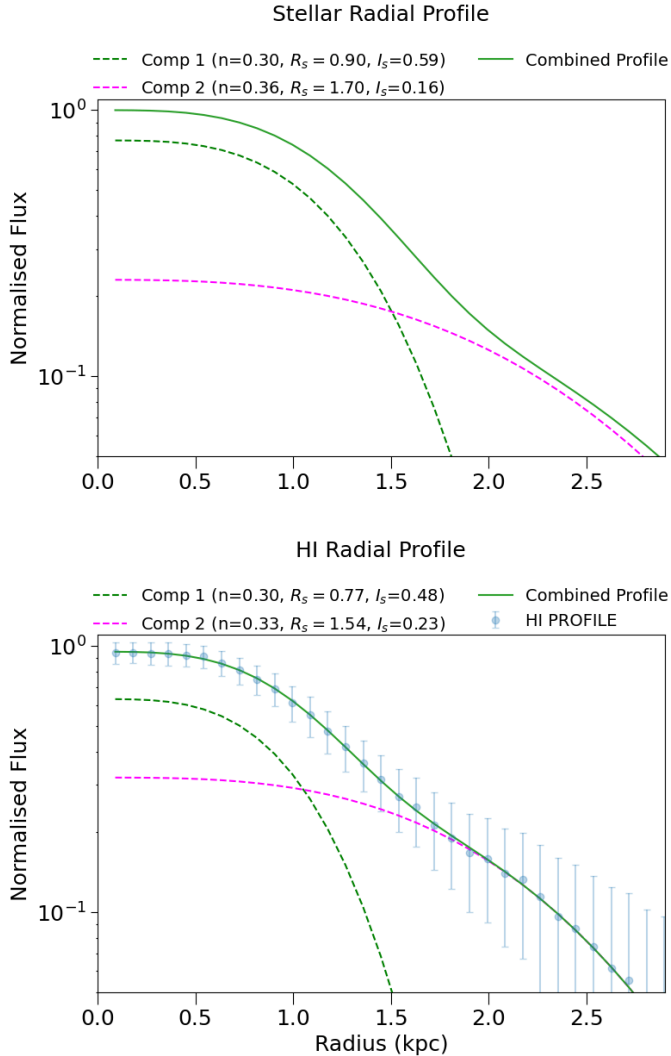


Fig. 4. Top: A reproduction of the two Sersic components of the stellar profile of WLM from Higgs et al. (2021). Bottom: Two Sersic components of the HI profile.

two halves of the disk separately owing to the asymmetry along the approaching and receding sides. All parameters are independently determined for both galaxy sides, which however share a common systemic velocity and center. The initial guesses for all parameters were used from Ianjamasimanana et al. (2020) and Kepley et al. (2007).

In the first iteration, we provide initial guesses for rotational velocity, dispersion, surface brightness, systemic velocity, position angle, inclination, dynamical center and thickness for 14 rings on both sides of the galaxy. Only the surface brightness, systemic velocity and dynamical center are allowed to vary and to arrive at a best fit in the first iteration.

Next, in the second iteration, we use the previously determined parameters as initial conditions, and let all of the mentioned parameters from the first iteration vary and then be determined further. Letting both the position and inclination vary all the way from the inner region to the outskirts should let us capture twist-like features in the galaxy. Then, to model non-circular motions, we fit for radial velocity and some second-order harmonics for velocity (RO2A, RO2P, RA2A, and RA2P in the TiRiFiC documentation) used by Spekkens & Sellwood (2007) to implement effects of bar streaming. Velocity harmon-

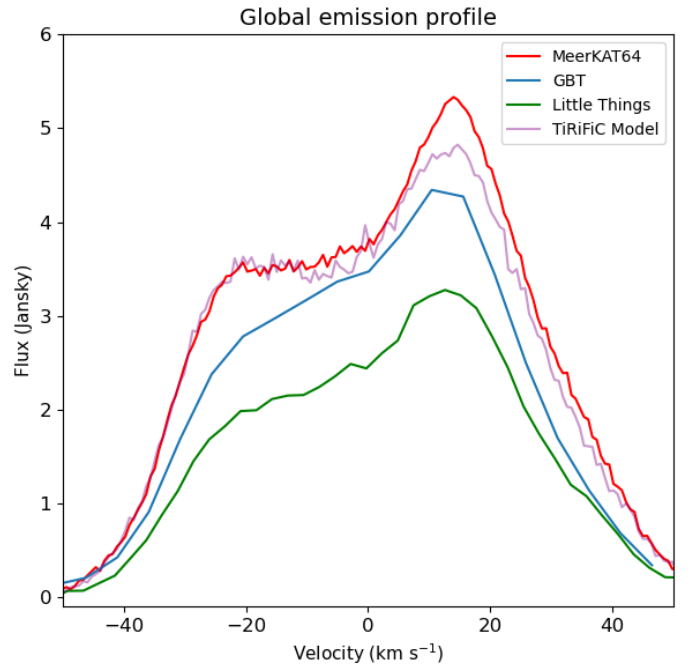


Fig. 5. Emission profile of the whole body of WLM from 3 major HI observations. The GBT observations are from the same data cube used in Ianjamasimanana et al. (2020), Little things VLA data is from Hunter et al. (2012). All observations were masked by SoFIA-2 and a common velocity range was set. Velocities are in the rest-frame .

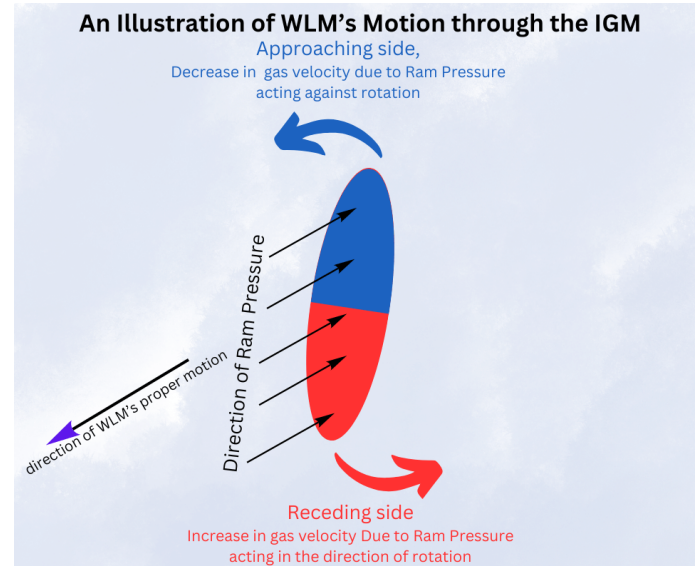


Fig. 6. An illustration of how WLM's motion through the IGM might affect its kinematics. As WLM moves through the IGM, the approaching side is slowing down as the ram pressure pushes against its rotation, while the receding side moves along the direction of ram pressure, and gains velocity, as it is seen in the rotation curves shown in Fig. 7

ics were also used by Ianjamasimanana et al. (2020) to successfully model non-circular motions in WLM. We then compare the PV diagram and global velocity profile of the model for consistency, and then proceed to double the number of rings to 28 to capture smaller variations and rerun the fit with all the previous fit parameters as initial conditions. The model is then pro-

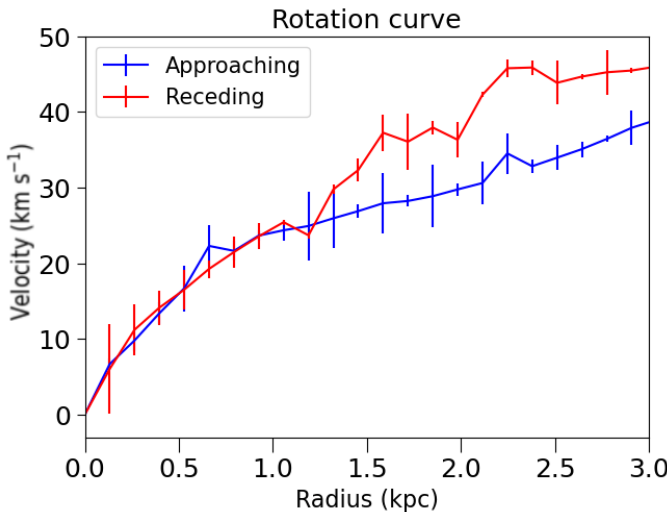


Fig. 7. Asymmetric drift corrected rotation curve of WLM along its approaching and receding sides. The rotation remains symmetric within the inner 1.5 kpc, beyond which the curves begin to diverge, suggesting that the gas is out of equilibrium, likely due to ram pressure effects..

cessed through TRMerrors¹ to obtain errors. Acquiring errors on all the parameters for every ring is very computationally expensive. Hence, we compute errors only on rotational velocity, dispersion, inclination and position angle, presented in Appendix A. Values for inclination and position angle presented in table 1 are average values of all the fits presented in Appendix A

Fig. 5 includes a comparison of the observed global velocity profile of WLM and of the TiRiFiC model obtained from the above procedure. The observation and the model seem to agree well. Comparing the PV diagrams of the model and the observation in Appendix B, we see that all observed features are recovered by the model, including the asymmetry between the approaching and receding sides as well as the 2 component-like split on the approaching side. We also provide moment maps and residuals for the TiRiFiC model in Appendix C.

Kepley et al. (2007) used a 2D method to obtain their rotation curves, and did not fit for dispersion and thickness. A similar prescription using TiRiFiC and velocity harmonics has been used to model WLM earlier by Ianjamasimanana et al. (2020), but they model both sides together with a single disk.

Our approach includes independent modelling of both sides, along with a fit for thickness, dispersion and velocity harmonics, leading to a comprehensive modelling of WLM. These new rotation curves seen in Fig. 7 for the approaching and receding sides, align well within the first kiloparsec, and do not show a divergence in the central region as it is seen in the Kepley et al. (2007) rotation curves.

In Sections 5 and 6, we discuss in detail about the inner component of WLM and the possibility of a bar-like structure in the center. Such a structure can provide inner disk velocity asymmetries, and contribute to non-circular motions, which we have considered and fit for in our TiRiFiC modelling. Sofue & Kohno (2025) report that for the rotation curve of the Milky Way along its inner bar region, the variation along two different regions of the Galaxy is 10-15%. If a similar impact were to be assumed for WLM, it would be 2-3 km s⁻¹ at 1.5 kiloparsec for our rotation curve. The asymmetry beyond 1.5 kiloparsec that has been found by Kepley et al. (2007) is consistent with our results.

¹ github.com/PeterKamphuis/TRM_errors

Beyond about 1.5 kiloparsec from the galaxy center, the restoring force is not strong enough from the galaxy center. Then, the approaching side loses velocity, and the receding side gains velocity as seen in the rotation curve's divergence shown in Fig. 7, and it confirms that ram pressure may explain the asymmetric RC of WLM (see Fig. 6). We observe an increased dispersion on the eastern edge of the galaxy, which can be seen in the moment-2 map of Fig. 2. This region is also visible in the residual moment 1 and 2 maps presented in Appendix C. This is also the side of the galaxy on which ram pressure is exerted, complex turbulent gas motions and ram pressure induced star formation may explain this increased dispersion.

When the rotation curve of a dwarf system does not exceed a few tens of km s⁻¹, it becomes essential to apply the asymmetric-drift correction. More specifically, for gas discs with ratios of rotational velocity to velocity dispersion as low as $V_{\text{rot}}/\sigma_v < 4$, pressure support can significantly affect the kinematics and must be taken into account using the so-called asymmetric-drift correction (Binney & Tremaine 2011; Bureau & Carignan 2002; Oh et al. 2011). We implement the procedure described by Oh et al. (2015). However, this correction is only necessary to estimate the dynamical mass of the galaxy under the assumption of equilibrium, which will be examined in a future paper. Corrected rotation curves are shown in Fig. 7, uncorrected ones are presented in Appendix A.

4.4. The shift of the gas dynamical center due to ram pressure

As described earlier, we let TiRiFiC find the dynamical center and systemic velocity in our iterative fitting procedure, common for all rings on either side of the galaxy, and it appears to be shifted by about 90 parsec from the stellar center in the direction of the ram pressure being applied to the galaxy, as reported in table 1. Further, we would like to note that the shift is within 1 beamsize and could be impacted by smearing.

Ram pressure is expected to more affect the dynamics of the low column density gas-disk outskirts, while gas in the inner region of the galaxy is denser and has experienced more orbits. For instance, looking at the PV diagram in Fig. 8 we can see that the rotational velocity is roughly 20 km s⁻¹ at 1 kpc, and we can estimate the number of orbits the gas has had at that radius to be 6.6 in 2 Gyr, while taking a rough velocity of 30 km s⁻¹ at 2.5 kpc we get ~ 4 orbits in 2 Gyr. Therefore, we expect the inner region to be more at dynamical equilibrium than the outer one, and we do confirm that the approaching and receding sides coincide in the inner region (see a discussion of galactic disk dynamics in Hammer et al. 2025). It is not uncommon for dwarf irregulars to have their HI centers slightly different from their optical centers derived from photometry (Patra et al. 2016). WLM seems substantially perturbed by ram pressure, with having lost 13% of its HI mass, just in the MeerKAT16 field of view, and this interaction may contribute to the shift of the dynamical center.

5. Kinematic Two-Component Decomposition

The global flux profile we present in Fig. 5 shows a strong peak at 10 km s⁻¹ and a plateau-like feature between 0 and -25 km s⁻¹. This suggests that there could be more than one rotating components in the gas body of WLM. Also, in the PV diagram presented in Fig. 8, on the approaching side we can see that the flux distribution also suggests the presence of two distinct kinematic branches. Further evidence for more than one component

could be seen if we observe the spectrum taken in the region beyond 1 kpc as seen in Fig. 8, which shows two distinct peaks, and indeed a two-component Gaussian fits much better to the spectrum in this region. On the receding side (Appendix D, row number 3), the second component may not be resolved, but the spectrum here is much broader than it is at the center of the PV diagram and is also better modeled by two components.

To systematically decompose our data cube into these two distinct components, we have applied the above method to every pixel in the data cube instead of just the central slice of the PV diagram. First, the original data cube has been re-binned by a factor 4:1 to increase the signal-to-noise ratio. We then extract the spectrum at every pixel in the data cube and fit two Gaussian profiles to the spectrum in each pixel in the data cube akin to the fit seen in Fig. 8 (see also Appendix D).

We segregate the components in two separate data cubes; at each pixel, we sort the component with the lower velocity of the two with respect to the systemic velocity into what we refer to as Component-1 and the larger velocity into what is referred to as Component-2. Beamsize smoothening kernel is applied to compensate for spurious fits from pixel to pixel. Then, we generate moment maps for these two components (see Fig. 9).

The reproduction of the datacube after this two-component decomposition can be seen in the second row of Fig. 10. We can see that it near perfectly reproduces the column density distribution of HI in the moment-0 map, as well as the velocity field in the moment-1 map. There are minor local variations from the observations in the moment-2 dispersion map, but the global features are well reproduced. We also compute rotation curves for each component using the methodology already used for the global rotation curve (see Section 4 and Fig. 11).

In Section 3, we obtained a 2 component Sersic fit on the total HI profile of WLM. This let us establish that the two components present in the stellar profile of WLM reported in Higgs et al. (2021) can be mapped onto the HI profile. Due to the high inclination of the disk, these components overlap in the global moment 0 map of WLM. The kinematic decomposition of the data lets us separate both the components cleanly, and obtain

moment maps presented in Fig. 9. We can now fit a single Sersic profile individually to the two kinematically separated components and compare them to the Sersic fits from Section 3. This comparison can be seen in Fig. 12. Both the kinematic decomposition and morphological decomposition show a compact inner component and a sparse outer component. Though in both cases the distinction between a compact and a sparse component is very clear, the Sersic parameters do not match perfectly, which is expected due to projection effects and the overlap between the two components. We discuss the properties of the two components in detail in Section 6.

We also obtained a global velocity profile for both components that we present in Fig. 13. Component-1 spans a smaller velocity range but contributes more to the sharp peak in the profile. This can be verified from the rotation curve, the velocity amplitude of this component is lower at all radii than that of Component-2. The latter is much more widely distributed in the velocity space, it extends beyond Component-1, and shows the differential rotation shape expected for a rotating disk which is the double horned profile. Fig. 13 shows that Component-2 has a slight velocity excess of few km s^{-1} on the receding side at about 40 km s^{-1} , which might be due to ram pressure.

6. Discussion

6.1. Inner Component-1

We now refer to Component-1 as the inner component of WLM. It has a half-light radius of 0.77 kpc in the morphological global profile decomposition presented in Section 3 and 1.11 kpc in the profile obtained after the kinematic decomposition in Section 5 and presented in Fig 12. For comparison, Component-2 is the outer component with a half-light radius of 1.53 kpc and 1.58 kpc in the global profile and kinematic decomposition results, respectively.

Gas in the moment-0 map for this component is more centrally packed, both along the major and minor axes. The central iso-velocity contours in the moment-1 map of Component-1 are oriented along a PA of about 165 degrees as seen in the

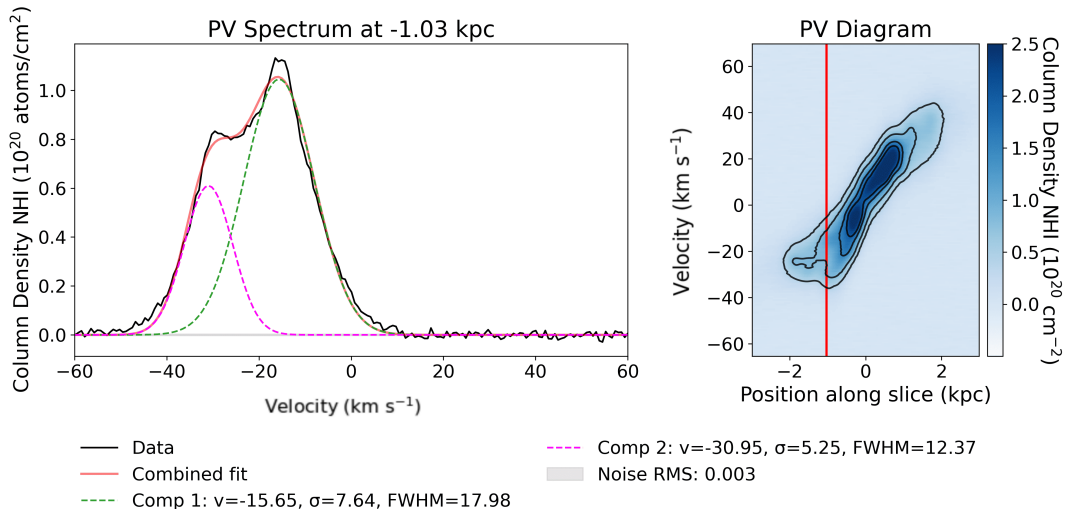


Fig. 8. One HI spectrum of WLM taken along the PV diagram. In the right panel, the vertical red line indicates the position at the PV diagram where the spectrum was taken. This slice shows 2 distinct peaks, modeled by 2 Gaussian fits corresponding to 2 different kinematic components. Parameters of the Gaussian fits are given on the bottom of the figure. Spectra around the center and receding side of the Galaxy are given in Appendix D.

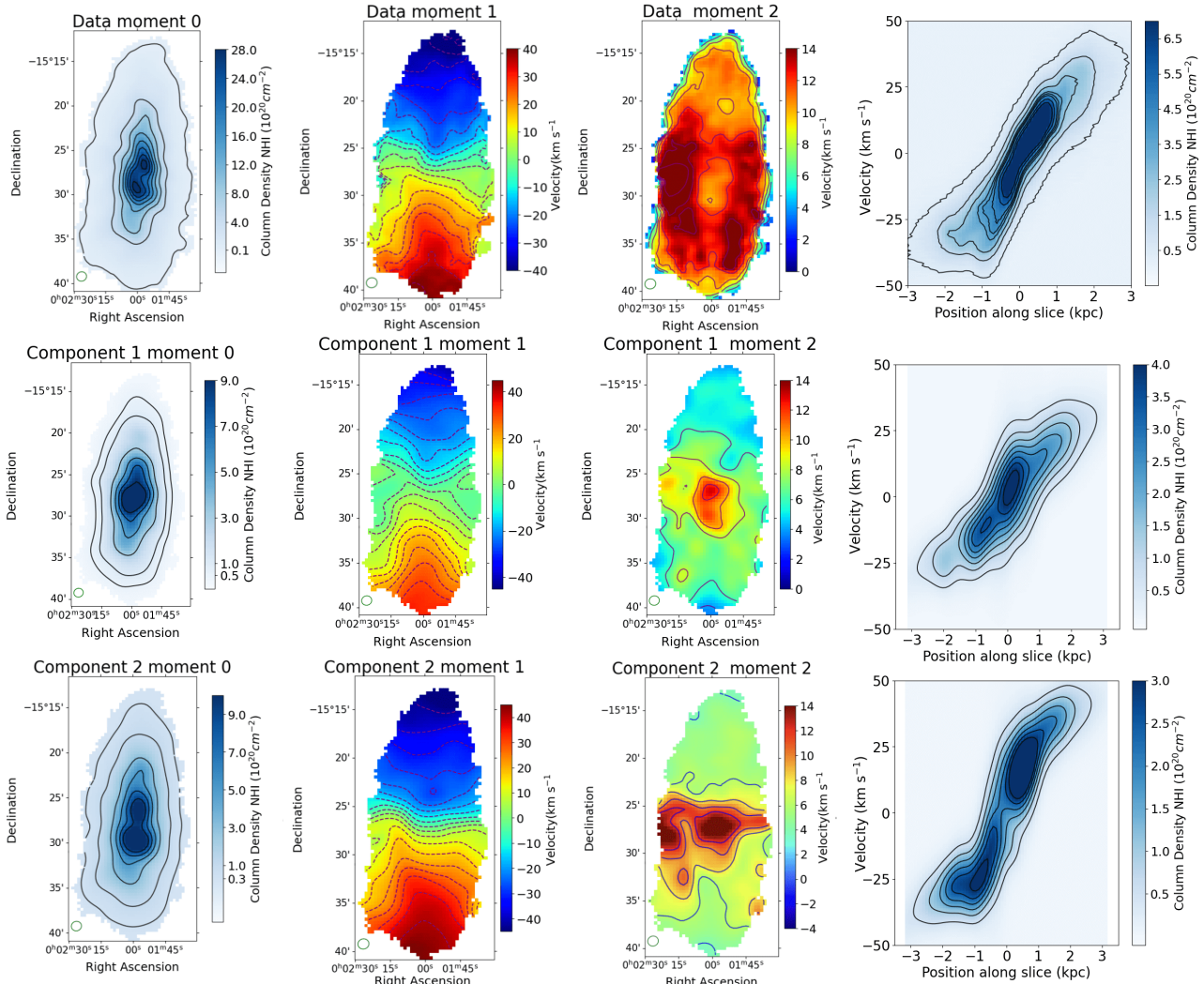


Fig. 9. First row shows the moment maps from our MeerKAT observations. Second row shows the moment maps of the slower component from our decomposition, which is also the central compact component. Row 3 has maps for the faster component, which is the more extended disk-like component. Each row is presented with a corresponding PV diagram at the right end. The contours on the moment-0 map and the PV diagram correspond to the ticks on the colour bar. The contours on the moment-1 map correspond to a velocity range between -40 to 40 km s⁻¹ with a spacing of 5 km s⁻¹ and for the moment-2 map they correspond to 6.9 and 12 km s⁻¹, respectively.

second row of Fig. 10, similar to the moment-1 map from the non-decomposed cube in the first row. In contrast, the inner velocity contours of Component-2 are nearly perpendicular to the PA of WLM. This suggests that we have successfully separated the component that contributes to the 165 degree contours in the global moment-1 map. This off-axis orientation also points towards this component's bar-like nature. The PV diagram for this component does not show any flattening at the outskirts and shows solid-body like increase in rotational velocity on both the approaching and receding sides all the way till at least 1.7 kpc. However, a careful examination of the PV diagram indicates a very central component, whose orientation is shifted from the overall PV diagram. This suggests component-1 to be more complex than a single bar. We will study the impact of such a structure on the dynamics of a galaxy like WLM interacting with the IGM in a future study with full hydrodynamical modelling. This is also seen in the rotation curve of this component. These bar-like motions contribute to the steep rotation curve in the inner regions. WLM is well known in the literature for a high star formation rate at the center of the galaxy (Albers et al. 2019). Along with the high inclination of WLM, this renders classi-

cal tests such as the Tremaine-Weinberg method for bars on a gas velocity field inconclusive (Hernandez et al. 2005). Gaseous bar-like structures have also been reported in several dwarf irregulars such as NGC 6822, NGC 3741, NGC 2915 and DDO 168 (Meurer et al. 1996; Banerjee et al. 2013; Patra & Jog 2019).

Anagha A.G. & Banerjee (2025) have also recently shown that gaseous bars can form and remain stable through hydrodynamical simulations. Another important feature which points towards a central bar-like structure is the distinct two-component split seen in the PV diagram. Bureau & Freeman (1999) show that a separate kinematic component can be a diagnostic for boxy peanut-shaped structures in galaxies. An ancillary support to the component to be a bar-like also comes from its Sersic index of 0.6, as A. Gadotti (2009) suggested that bars usually have Sersic indices between 0.5-1.

6.2. Outer Component-2

The outer Component-2 in both the morphological and kinematic decomposition shows extended and disk-like features. It seems to trace a more spread-out component of the gas distribu-

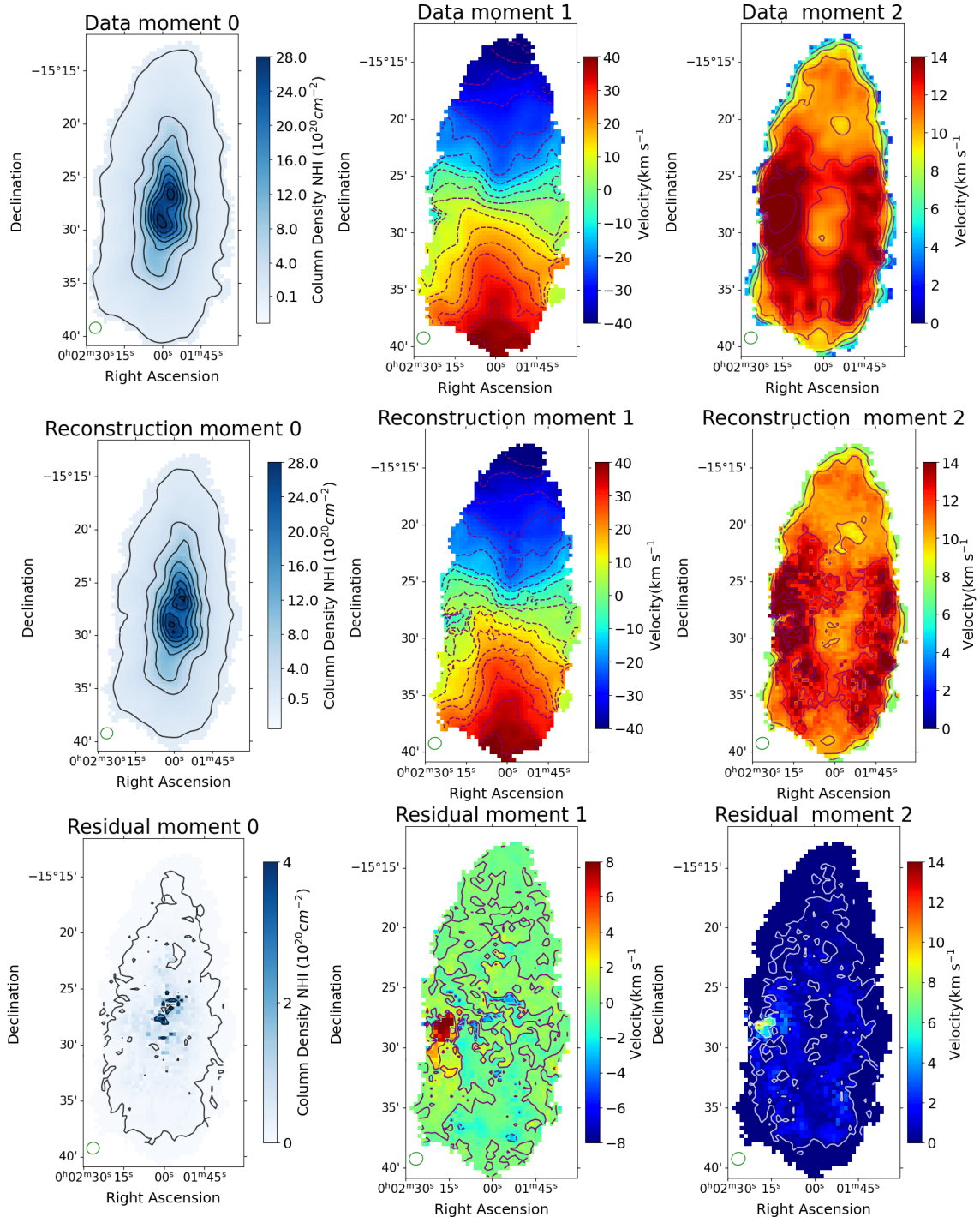


Fig. 10. The first row shows moment maps of the Meerkat dish 64 observations, the second row shows our combined two-component model which reproduces most of the features in observed moment maps, the bottom row shows the residuals from the subtraction of the two. The contours of moment-0 map correspond to the ticks of the colourbar. The contours on the moment-1 map correspond to a velocity range between -40 to 40 km s⁻¹ with a spacing of 5 km s⁻¹ and for the moment-2 map they correspond to 6,8,10,12,14 km s⁻¹, respectively.

tion along the major and minor axes of the galaxy. Looking at the velocity field we see that at inner radii, we have a rapid increase in velocity on both sides of the galaxy, which progressively evolve into V-shaped contours often seen in galactic disks. The central iso-velocity contours in the moment-1 map are nearly perpendicular to the PA = 175 degree major axis, indicating clear distinction from the off-axis bar-like Component-1. The dispersion of this component decreases progressively from the center to the outskirts; such steady variation is often seen in galac-

tic disks supporting the validity of our decomposition (Hammer et al. 2017). The classical double-horn profile, which is the kinematic signature of HI rotating disks is seen in Component-2 is seen in Fig. 13. The two horns correspond to the outer parts of the disk where the rotation curve is flat, producing a large contribution at the maximum projected velocities. The relative dip near the systemic velocity arises because gas at central velocities comes from smaller radii and contributes less to the total flux. In addition, the double-horn shape becomes more distinct and

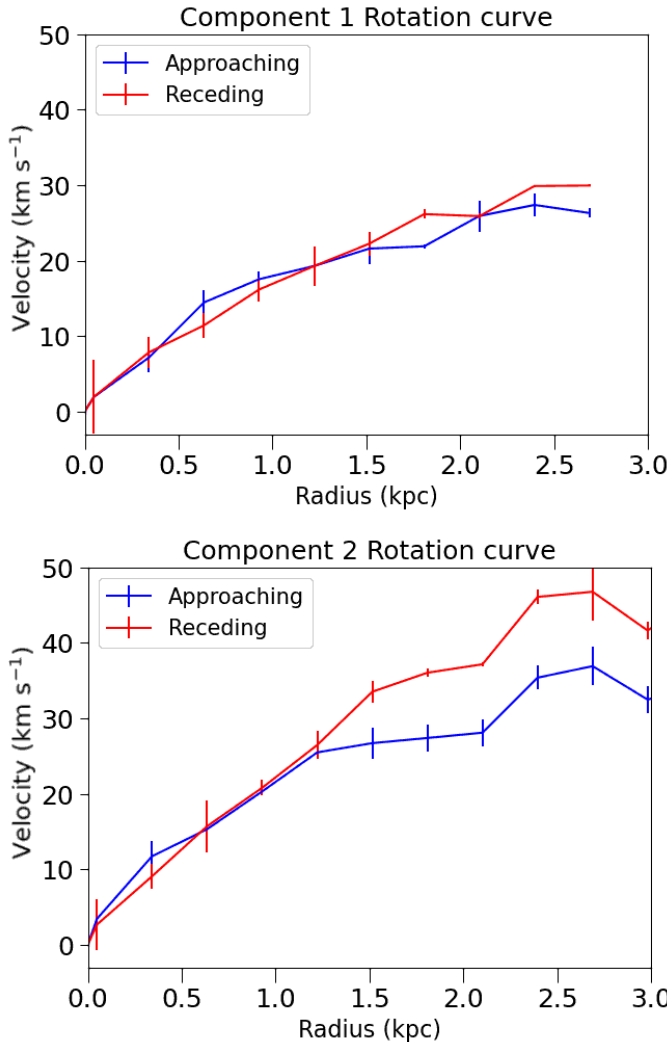


Fig. 11. Rotation curves of each individual component. Component-1 shows a solid body like rotation curve which seems not affected by ram pressure. The disk-like Component-2 shows a strong divergence beyond 1 kpc and is likely perturbed by ram pressure.

stronger as galaxies are viewed closer to edge-on where the observed line-of-sight velocities closely reflect the true rotational velocities (Giovanelli & Haynes 1988). In the PV diagram for this component in Fig. 9 we can clearly see velocities flattening beyond one kiloparsec on the approaching side, which is also seen in its rotation curve in Fig. 11.

Component-2 is sparse at the outer edges, and it seems to have been perturbed by ram pressure, which appears to be responsible of the rotation curve asymmetry observed in the global rotation curve.

7. Conclusions

WLM is a Local-group gas-rich dwarf irregular whose gas kinematics and dynamics are perturbed by ram pressure effects exerted by the surrounding IGM. Yang et al. (2022) showed that WLM is continuously losing gas as it travels through the IGM. Our revised MeerKAT-16 moment maps show that 13 % of the total gas mass has been presently lost from the main body just in the field of view. Considering that WLM is a gas-rich and star-forming dwarf galaxy at the current epoch, its dynamics was likely dominated by gas motions in the past. Using our new

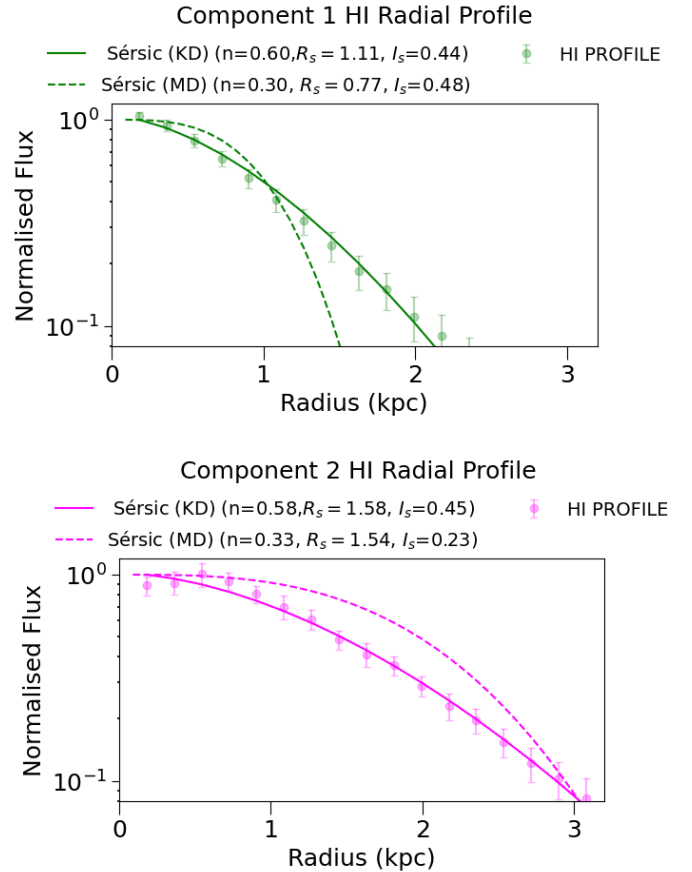


Fig. 12. 1D HI profiles of the kinematically decomposed (KD) components fit with a Sersic profile with Sersic parameters presented on the top of each panel. We have over-plotted with dashed lines the Sersic profile from our morphological decomposition (MD) from section 3. .

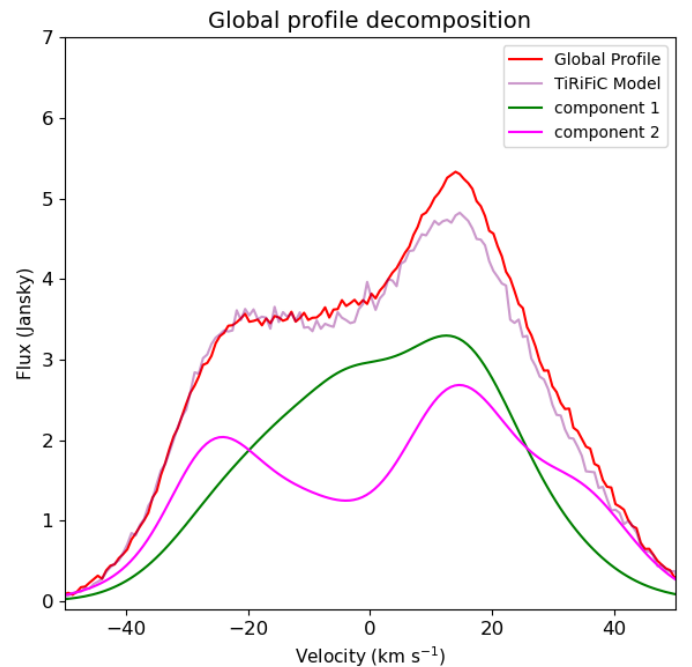


Fig. 13. Emission profile of the whole body of WLM with the contributions from the two components along with the profile of the TiRiFiC model.

high-resolution MeerKAT 64 observations, we have been able to show that the gas kinematics of WLM beyond 1.5 kiloparsec is severely impacted by its motion through the IGM, consequently affecting the rotation curve and any subsequent mass estimates from it.

Our morphological and kinematic decomposition shows that WLM appears to have an inner bar-like structure which is identified by its solid-body inner rotation curve, which seems more resilient to perturbations, while the disk-like outer component is characterized by a double-horn profile. The latter component is severely impacted by ram pressure effects, which contribute to the rotation curve asymmetry between the receding and the approaching sides.

Dynamical studies of dwarf galaxies often focus on isolated bodies with minimal tidal interactions to better understand their internal structure in order to estimate their total mass. Here we find that dwarf motions with respect to the local IGM can generate ram-pressure effects sufficiently strong to affect the gas dynamics at the outskirts of their disks. It suggests that more consideration must be given to understand the distribution and density of the ionized medium through which galaxies travel.

In the near future, we will present detailed hydrodynamic simulations in an attempt to model WLM and its interaction with the IGM to further probe the above scenario and further probe how ram pressure affects the galaxy differentially. The local group IGM is sparse enough to be undetected by present-day direct observations. Accurately modeling WLM and its interaction with the medium will allow us to put realistic constraints on the local IGM density as well as on the WLM total mass estimate.

Acknowledgements. Authors RI and BN acknowledge financial support from the grant PID2021-123930OB-C21 funded by MICIU/AEI/10.13039/501100011033 and by ERDF/EU, and the grant CEX2021-001131-S funded by MICIU/AEI/ 10.13039/501100011033, and the grant TED2021-130231B-I00 funded by MICIU/AEI/ 10.13039/501100011033 and by the European Union NextGenerationEU/PRTR, and the grant INFRA24023 (CSIC4SKA) funded by CSIC, and acknowledge the Spanish Prototype of an SRC (espSRC) service and support funded by the Ministerio de Ciencia, Innovacion y Universidades (MICIU), by the Junta de Andalucia, by the European Regional Development Funds (ERDF) and by the European Union NextGenerationEU/PRTR. The espSRC acknowledges financial support from the Agencia Estatal de Investigacion (AEI) through the Center of Excellence Severo Ochoa award to the Instituto de Astrofisica de Andalucia (IAA-CSIC) (SEV-2017-0709) and from the grant CEX2021-001131-S funded by MICIU/AEI/ 10.13039/501100011033. Part of BN work was supported by the grant PTA2023-023268-I funded by MICIU/AEI/ 10.13039/501100011033 and by ESF+. The MeerKAT telescope is operated by the South African Radio Astronomy Observatory, which is a facility of the National Research Foundation, an agency of the Department of Science and Innovation.

References

A. Gadotti, D. 2009, in *Chaos in Astronomy*, ed. G. Contopoulos & P. A. Patsis (Berlin, Heidelberg: Springer Berlin Heidelberg), 159–172

Albers, S. M., Weisz, D. R., Cole, A. A., et al. 2019, *Monthly Notices of the Royal Astronomical Society*, 490, 5538

Anagha A.G., A. & Banerjee, A. 2025, *The Astrophysical Journal*, 983, 94

Archer, H. N., Hunter, D. A., Elmegreen, B. G., et al. 2022, *The Astronomical Journal*, 163, 141

Banerjee, A., Patra, N. N., Chengalur, J. N., & Begum, A. 2013, *Monthly Notices of the Royal Astronomical Society*, 434, 1257

Battaglia, G., Taibi, S., Thomas, G. F., & Fritz, T. K. 2022, *Astronomy & Astrophysics*, 657, A54

Binney, J. & Tremaine, S. 2011, *Galactic dynamics* (Princeton university press)

Bureau, M. & Carignan, C. 2002, *AJ*, 123, 1316

Bureau, M. & Freeman, K. C. 1999, *AJ*, 118, 126

Burnham, K. P., Anderson, D. R., & Anderson, D. R. 2010, *Model selection and multimodel inference: a practical information-theoretic approach*, 2nd edn. (New York, NY: Springer)

Carignan, C. & Freeman, K. C. 1988, *ApJ*, 332, L33

Connor, L., Ravi, V., Sharma, K., et al. 2025, *Nature Astronomy*

de Blok, W. J. G., Walter, F., Brinks, E., et al. 2008, *The Astronomical Journal*, 136, 2648, publisher: American Astronomical Society

Garrido, J., Darriba, L., Sánchez-Expósito, S., et al. 2021, *Journal of Astronomical Telescopes, Instruments, and Systems*, 8, 1

Giovanelli, R. & Haynes, M. P. 1988, in *Galactic and Extragalactic Radio Astronomy*, ed. K. I. Kellermann & G. L. Verschuur, 522–562

Hammer, F., Puech, M., Flores, H., & Rodrigues, M. 2017, *Studying Distant Galaxies (WORLD SCIENTIFIC (EUROPE))*

Hammer, F., Wang, J., Mamon, G. A., et al. 2024, *Monthly Notices of the Royal Astronomical Society*, 527, 2718, publisher: Oxford University Press (OUP)

Hammer, F., Yang, Y. B., Amram, P., et al. 2025, *Astronomy & Astrophysics*, 694, A16

Hernandez, O., Wozniak, H., Carignan, C., & Amram, P. 2005

Higgs, C. R., McConnachie, A. W., Annau, N., et al. 2021, *Monthly Notices of the Royal Astronomical Society*, 503, 176

Hunter, D. A., Ficut-Vicas, D., Ashley, T., et al. 2012, *The Astronomical Journal*, 144, 134

Ianjamasimanana, R., Namumba, B., Ramaila, A. J. T., et al. 2020, *Monthly Notices of the Royal Astronomical Society*, 497, 4795

Ianjamasimanana, R., Walter, F., De Blok, W. J. G., Heald, G. H., & Brinks, E. 2018, *The Astronomical Journal*, 155, 233, publisher: American Astronomical Society

Jin, X., Yang, J., Fan, X., et al. 2023, *The Astrophysical Journal*, 942, 59, publisher: American Astronomical Society

Jonas, J. 2018, in *Proceedings of MeerKAT Science: On the Pathway to the SKA — PoS(MeerKAT2016)*, Vol. 277, 001

Józsa, G. I. G., Kenn, F., Klein, U., & Oosterloo, T. A. 2007, *A&A*, 468, 731

Józsa, G. I. G., White, S. V., Thorat, K., et al. 2020, in *ASP Conf. Ser.*, Vol. 527, *ADASS XXIX*, ed. R. Pizzo, E. Deul, J.-D. Mol, J. de Plaa, & H. Verkouter, San Francisco, 635–638

Kepley, A. A., Wilcots, E. M., Hunter, D. A., & Nordgren, T. 2007, *The Astronomical Journal*, 133, 2242

Khademi, M., Yang, Y., Hammer, F., & Nasiri, S. 2021, *Astronomy & Astrophysics*, 654, A7

Li, P., Liu, A., Kluge, M., et al. 2024, *Astronomy & Astrophysics*, 692, A253, publisher: EDP Sciences

McClure-Griffiths, N. M., Pisano, D. J., Calabretta, M. R., et al. 2009, *ApJS*, 181, 398

McConnachie, A. W. 2012, *The Astronomical Journal*, 144, 4

McConnachie, A. W., Venn, K. A., Irwin, M. J., Young, L. M., & Geehan, J. J. 2007, *The Astrophysical Journal*, 671, L33

McQuinn, K. B. W., B. Newman, M. J., Savino, A., et al. 2024, *The Astrophysical Journal*, 961, 16

Meurer, G. R., Carignan, C., Beaulieu, S. F., & Freeman, K. C. 1996, *AJ*, 111, 1551

Mondal, C., Subramaniam, A., & George, K. 2018, *The Astronomical Journal*, 156, 109

Offringa, A. R., McKinley, B., Hurley-Walker, N., et al. 2014, *MNRAS*, 444, 606

Oh, S.-H., de Blok, W. J. G., Brinks, E., Walter, F., & Kennicutt, R. C. 2011, *The Astronomical Journal*, 141, 193

Oh, S.-H., Hunter, D. A., Brinks, E., et al. 2015, *AJ*, 149, 180

Patra, N. N., Chengalur, J. N., Karachentsev, I. D., & Sharina, M. E. 2016, *FIGGS2: An HI survey of extremely faint irregular galaxies*, arXiv:1609.01072 [astro-ph]

Patra, N. N. & Jog, C. J. 2019, *Monthly Notices of the Royal Astronomical Society*, 488, 4942

Read, J. I., Iorio, G., Agertz, O., & Fraternali, F. 2017, *Monthly Notices of the Royal Astronomical Society*, stx147

Roberts, I. D., Van Weeren, R. J., McGee, S. L., et al. 2021, *Astronomy & Astrophysics*, 650, A111

Serra, P., Westmeier, T., Giese, N., et al. 2015, *Monthly Notices of the Royal Astronomical Society*, 448, 1922

Sofue, Y. & Kohno, M. 2025, *PASJ*[arXiv:2509.23581]

Spekkens, K. & Sellwood, J. A. 2007, *ApJ*, 664, 204

Teodoro, E. M. D. & Fraternali, F. 2015, *Monthly Notices of the Royal Astronomical Society*, 451, 3021

Wang, J., Hammer, F., Yang, Y., et al. 2024, *Monthly Notices of the Royal Astronomical Society*, 527, 7144, publisher: Oxford University Press (OUP)

Westmeier, T., Kitaeff, S., Pallot, D., et al. 2021, *MNRAS*, 506, 3962

Westmeier, T., Kitaeff, S., Pallot, D., et al. 2021, *Monthly Notices of the Royal Astronomical Society*, 506, 3962

Yang, Y., Ianjamasimanana, R., Hammer, F., et al. 2022, *Astronomy & Astrophysics*, 660, L11

Appendix A: Radial variation in tilted rings fit parameters

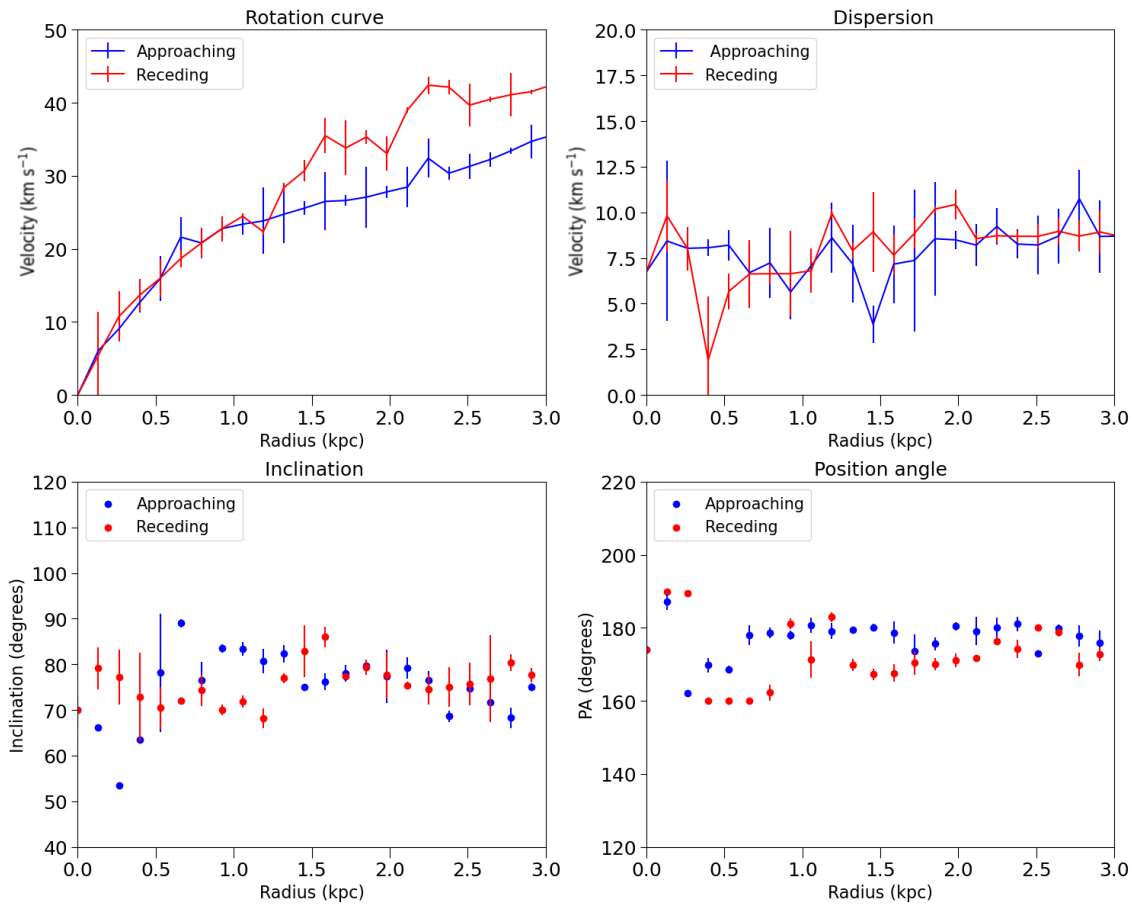


Fig. A.1. Subplots show the variation in the fit Rotation velocity, dispersion, Inclination and position angle of the tilted rings fit described in Section 4. The velocities here are not corrected for asymmetric drift

Appendix B: Comparing PV diagrams: Observations Vs Model

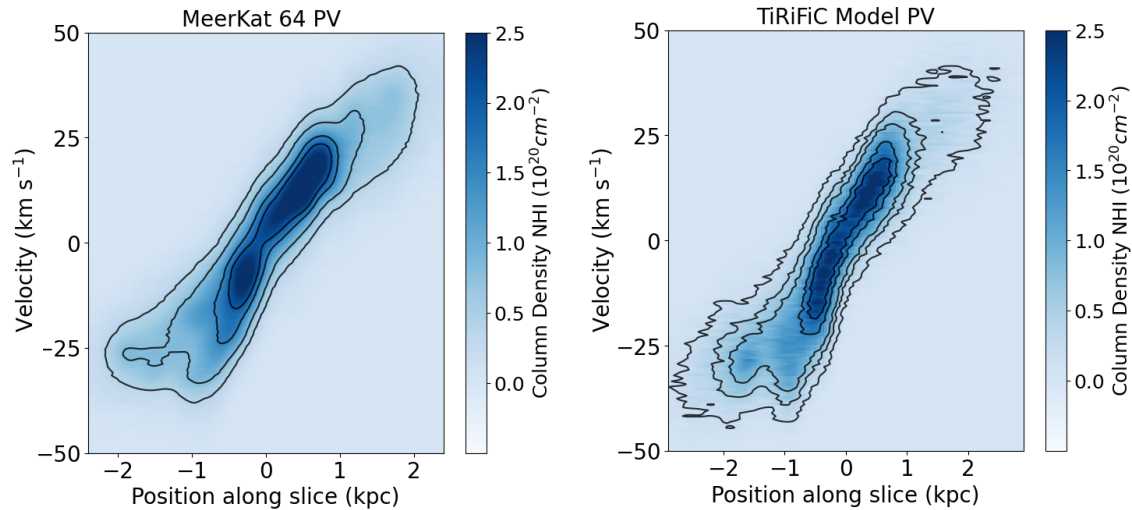


Fig. B.1. A comparison of PV diagrams from the MeerKAT observations on the left and the TiRiFiC model on the right. Contours correspond to ticks on the colourbar

Appendix C: TiRiFiC Model Moment Maps and Residuals

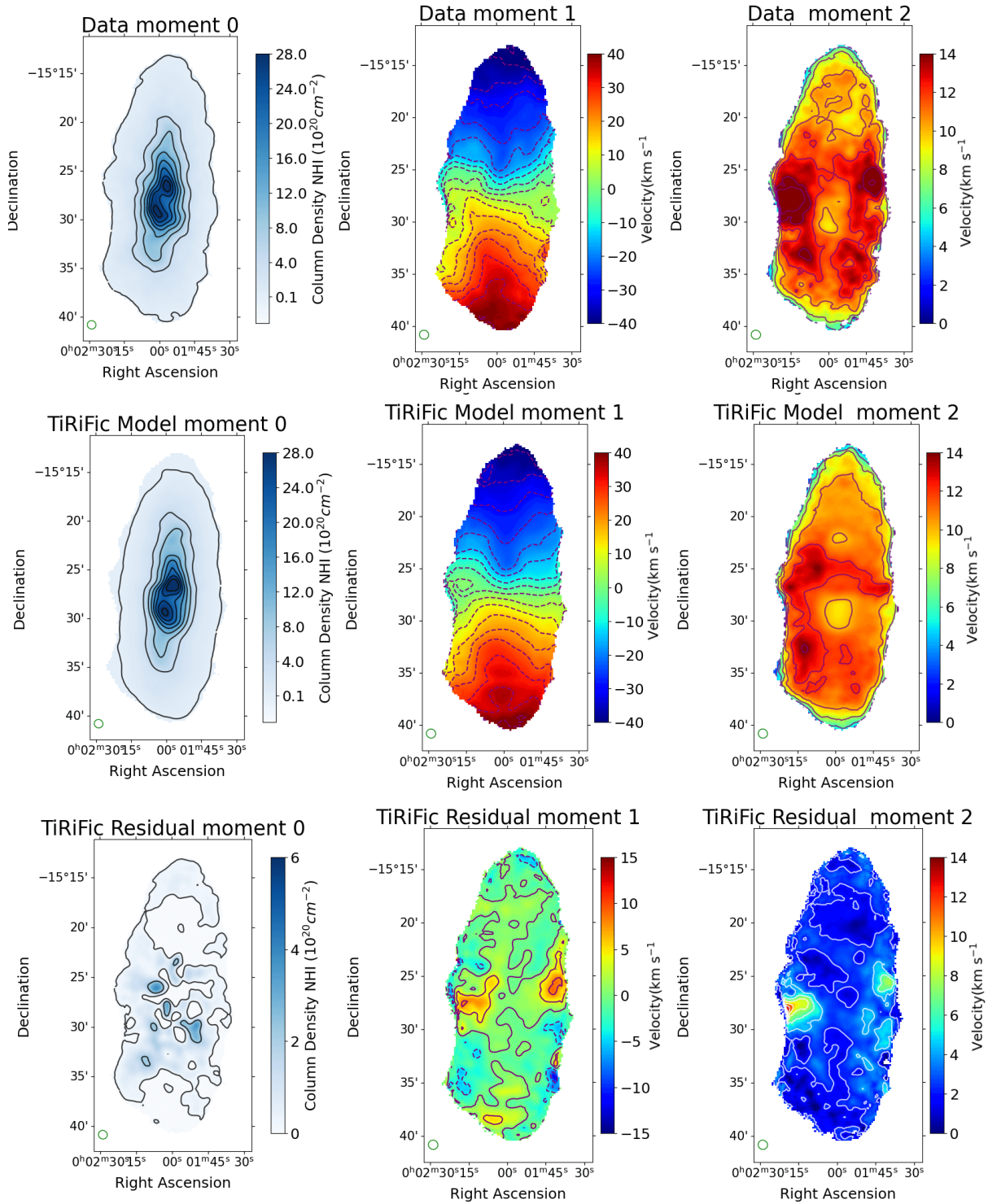


Fig. C.1. Contours in the first 2 rows and all moment 0 maps follow the same structure as described in Fig. 10. For the residuals in row 3 the contours on the moment 1 map correspond to -12 to 12 km s^{-1} with an increment of 4 km s^{-1} and for the moment 2 map in the same row they correspond to the ticks on the colourbar

Appendix D: Other slices of the PV diagram

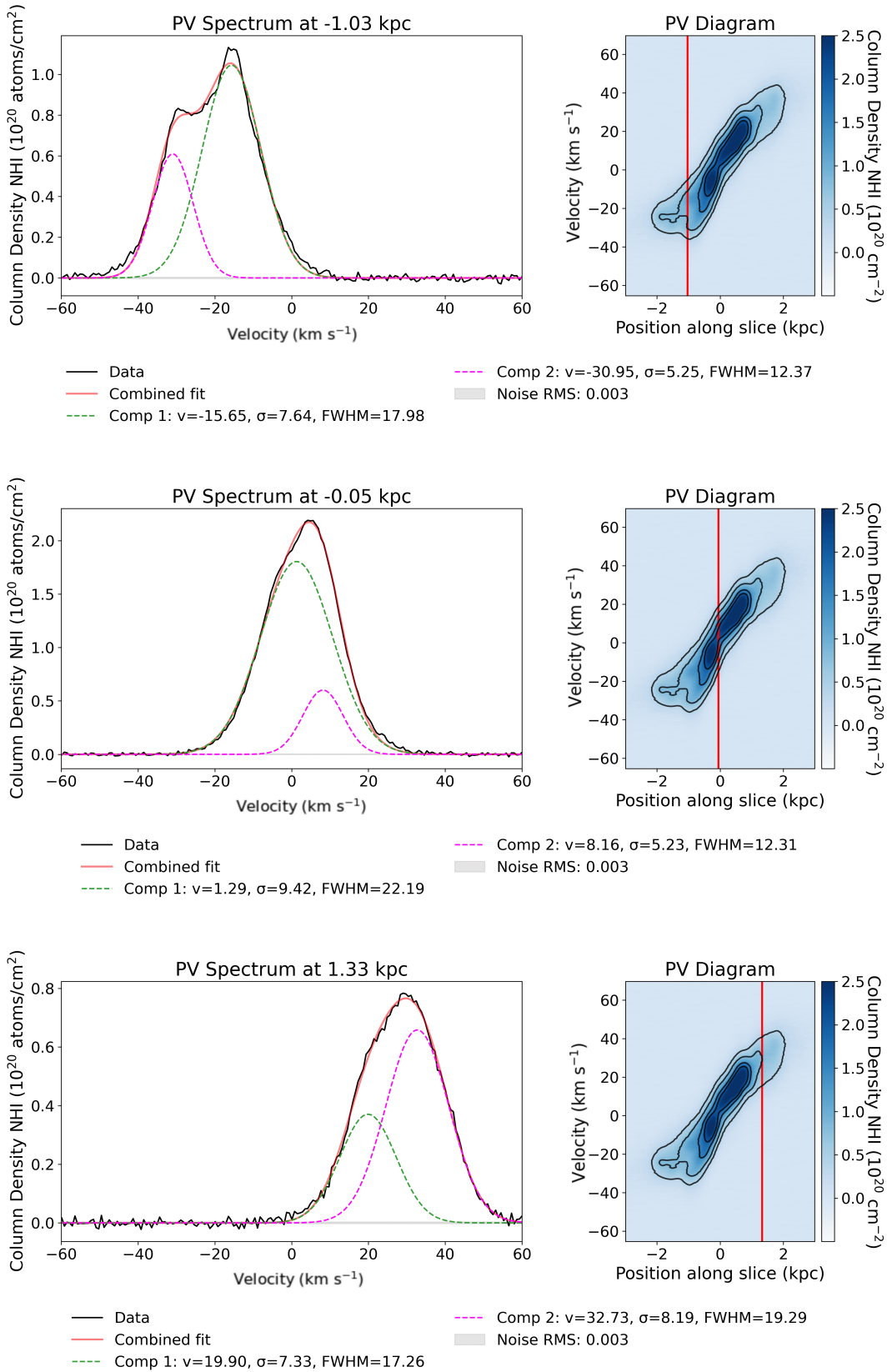


Fig. D.1. Spectra along 3 different slices of the PV diagram along with two-component decomposition. Same symbols as in Fig. 8.